Nominal Waveforms for Late-Time High-Altitude Electromagnetic Pulse (HEMP)

DTRA-TR-19-41

A Technical Report Submitted by:

Applied Research Associates, Inc.

September 2019

REPORT DOCUMENTATION PAGE

1. REPORT DATE *(DD-MM-YYYY)* 27-09-2019	2. REPORT TYPE Technical Report	3. DATES COVERED *(From - To)* March 2019 – September 2019

4. TITLE AND SUBTITLE
Nominal Waveforms for Late-Time High-Altitude Electromagnetic Pulse (HEMP)

5a. CONTRACT NUMBER
HDTRA1-14-D-0003-0030

5b. GRANT NUMBER

5c. PROGRAM ELEMENT NUMBER

6. AUTHOR(S)
Keith Siebert
Earl Witt

5d. PROJECT NUMBER
D00045.00016.02001

5e. TASK NUMBER

5f. WORK UNIT NUMBER

7. PERFORMING ORGANIZATION NAME(S) AND ADDRESS(ES) AND ADDRESS(ES)
Applied Research Associates
39 Simon St Suite 15
Nashua, NH 03062

8. PERFORMING ORGANIZATION REPORT NUMBER

9. SPONSORING / MONITORING AGENCY NAME(S) AND ADDRESS(ES)
Defense Threat Reduction Agency/RD-NTE
8725 John J. Kingman Rd., MSC 6201
Ft. Belvoir, VA 22060-6201

10. SPONSOR/MONITOR'S ACRONYM(S)
DTRA/RD-NTE

11. SPONSOR/MONITOR'S REPORT NUMBER(S)
DTRA-TR-19-41

12. DISTRIBUTION / AVAILABILITY STATEMENT

13. SUPPLEMENTARY NOTES

14. ABSTRACT
The report explores the late-time, high-altitude electromagnetic pulse, referred to as HEMP E3, using unclassified yields and X-ray outputs. The report shows how predicted HEMP E3 varies with yield, height of burst, and latitude, and provides electric-field waveforms at fixed and time-varying spatial locations (the latter to illustrate the peak value across the affected spatial domain).

15. SUBJECT TERMS
Electromagnetic Pulse · EMP · High-Altitude EMP · Waveforms · Late-Time HEMP · HEMP E3

16. SECURITY CLASSIFICATION OF:			17. LIMITATION OF ABSTRACT UU	18. NUMBER OF PAGES	19a. NAME OF RESPONSIBLE PERSON Mark L. Sward
a. REPORT UNCLASSIFIED	**b. ABSTRACT** UNCLASSIFIED	**c. THIS PAGE** UNCLASSIFIED		23	**19b. TELEPHONE NUMBER** *(include area code)* 703-767-2525

UNIT CONVERSION TABLE
U.S. customary units to and from international units of measurement[1]

U.S. Customary Units	Multiply by → ← Divide by[2]		International Units
Length/Area/Volume			
Inch (in)	2.54	$\times 10^{-2}$	Meter (m)
Foot (ft)	3.048	$\times 10^{-1}$	Meter (m)
Yard (yd)	9.144	$\times 10^{-1}$	Meter (m)
Mile (mi, international)	1.609 344	$\times 10^{3}$	Meter (m)
Nautical Mile (nmi, nautical, U.S.)	1.852	$\times 10^{3}$	Meter (m)
Barn (b)	1	$\times 10^{-28}$	Square Meter (m^2)
Gallon (gal, U.S. liquid)	3.785 412	$\times 10^{-3}$	Cubic Meter (m^3)
Cubic Foot (ft^3)	2.831 685	$\times 10^{-2}$	Cubic Meter (m^3)
Mass/Density			
Pound (lb)	4.535 924	$\times 10^{-1}$	Kilogram (kg)
Unified Atomic Mass Unit (amu)	1.660 539	$\times 10^{-27}$	Kilogram (kg)
Pound-Mass per Cubic Foot (lb ft^{-3})	1.601 846	$\times 10^{1}$	Kilogram per cubic meter (kg m^{-3})
Pound-Force (lbf avoirdupois)	4.448 222		Newton (N)
Energy/Work/Power			
Electron Volt (eV)	1.602 177	$\times 10^{-19}$	Joule (J)
Erg	1	$\times 10^{-7}$	Joule (J)
Kiloton (kT) (TNT equivalent)	4.184	$\times 10^{12}$	Joule (J)
British Thermal Unit (BTU) (thermochemical)	1.054 350	$\times 10^{3}$	Joule (J)
Foot-Pound-Force (ft lbf)	1.355 818		Joule (J)
Calorie (cal) (thermochemical)	4.184		Joule (J)
Pressure			
Atmosphere (atm)	1.013 250	$\times 10^{5}$	Pascal (Pa)
Pound Force per Square Inch (psi)	6.984 757	$\times 10^{3}$	Pascal (Pa)
Temperature			
Degree Fahrenheit (°F)	[T(°F) − 32]/1.8		Degree Celsius (°C)
Degree Fahrenheit (°F)	[T(°F) + 459.67]/1.8		Kelvin (K)
Radiation			
Curie (Ci) [Activity of Radionuclides]	3.7	$\times 10^{10}$	Per Second (s^{-1}) [becquerel (Bq)]
roentgen (R) [air exposure]	2.579 760	$\times 10^{-4}$	Coulomb per Kilogram (C kg^{-1})
rad [absorbed dose]	1	$\times 10^{-2}$	Joule per Kilogram (J kg^{-1}) [gray (Gy)]
rem [equivalent and effective dose]	1	$\times 10^{-2}$	Joule per Kilogram (J kg^{-1}) [Sievert (Sv)]

[1]Specific details regarding the implementation of SI units may be viewed at http://www.bipm.org/en/si/.

[2]Multiply the U.S. customary unit by the factor to get the international unit. Divide the international unit by the factor to get the U.S. customary unit.

Table of Contents

List of Tables

No table of figures entries found.

List of Figures

1 INTRODUCTION

1.1 Physics

E3, also referred to as late-time EMP or magnetohydrodynamic (MHD) EMP, is the third phase of High-Altitude EMP (HEMP) generated by a high-altitude nuclear burst. Whereas the first two phases of HEMP, E1 and E2, are caused by prompt gamma and neutron emissions, the dominant driver for E3 is motion of burst-generated plasma perpendicular to the ambient geomagnetic field. Because burst-generated plasma is highly conducting, magnetic fields lines are "frozen" within it, so plasma motions act to distort magnetic field lines. This creates electric currents and time-dependent magnetic fields that propagate as electromagnetic waves down to and into the ground. The two most important plasma motions are [1] the outward expansion of plasma from the burst point creating a magnetic bubble, and [2] the rise of plasma due to heave of burst-heated atmosphere that drags magnetic field lines upward. These motions further subdivide the E3 signal into two sub-categories, E3A and E3B. E3A is often referred to as the "blast-wave" signal and E3B as the "heave" signal.

Historically, E3A refers specifically to the E3 signal generated by collisionless expansion of weapon debris from the burst point, and is thus only important for burst-altitudes above ~250 km. The magnetic bubble created by collisionless debris expansion evolves on a time scale of ~10 seconds. For example, the magnetic bubble created by the Starfish atmospheric test (burst altitude of 400 km) reached maximum extent in about 1 second, and then collapsed after 16 seconds [1]. A high-altitude nuclear explosion (HANE) can also create an additional magnetic bubble driven by collisional energy deposition processes. In the case of Starfish-regime burst altitudes, air ions energized by the collisionless blast wave stream down magnetic fields lines and deposit their energy in an ionization region known as the kinetic energy patch (KEP). At lower burst altitudes (90 to 250 km), UV photons emitted from a collisional blast wave form a hot-plasma sphere known as the UV fireball. In both cases, subsequent expansion of the resulting plasma creates a magnetic bubble that will also generate its own E3 signal. Hot plasma magnetic bubbles expand on time scales of several 10s of seconds to a minute, and thus evolve on significantly longer time scales than their collisionless counterparts. So even though the phenomenology of the hot-plasma magnetic bubble is "E3A-like", its time scale is more "E3B-like." For this reason, we categorize the E3 signal from hot plasma magnetic bubbles as being part of E3B and not E3A.

This report focuses on E3B for burst-altitudes from 90 to 250 km. We will provide a set of unclassified E3B waveforms and demonstrate their dependence on yield, burst-altitude, and burst-latitude. We will also provide a discussion on the physics that determines these dependencies.

1.2 Analogy to Geomagnetic Storms

E3 generation is analogous to the physics that governs naturally occurring geomagnetically induced currents (GIC). GICs are a manifestation of space weather events known as geomagnetic storms that enhance ionospheric current systems and induce electric fields in the ground. Since ionospheric current systems are strongest near the magnetic pole, GICs are primarily high-latitude events, although sufficiently strong storms can drive GICs at lower latitudes. A key difference between naturally occurring GIC and E3 is the atmospheric environment through which their respective electromagnetic signals propagate. This is because in addition to a hot plasma region, a HANE creates ionization layers below the burst point that alter electromagnetic propagation. Two

important layers are the X-ray patch and the beta patch. The X-ray patch is created by absorption of X-rays emitted almost instantaneously after detonation. For burst altitudes greater than ~90 km, X-ray absorption is largest in the higher density air below the burst and peak ionization generally occurs between 80 and 100 km altitude. The X-ray patch can have horizontal extents of several hundred to thousands of km from the burst vertical. Conductivity in the X-ray patch acts to shield burst-generated electromagnetic signals from the ground below. These signals must either diffract around the edges of the X-ray patch or diffuse through it, thus altering both the magnitude and timing of the ground signal. The beta patch is a much more horizontally-localized ionization region below the burst point. It is created by beta-electrons from radioactive decay of fission products. These electrons spiral down magnetic field lines toward lower-altitude air where they are absorbed. Ionization from beta absorption is generally peaked around altitudes of 60 – 70 km.

1.3   Longmire Analysis of E3 Waveform

Conrad Longmire analyzed magnetometer measurements from the Fishbowl series of high altitude nuclear tests and identified common characteristics of measured magnetic field waveforms [2]. Figure 1 shows the E3 magnetic field waveform taken on Johnston Island during the Starfish test. It is important to note that the magnetometers fielded at Johnston Island only measured the total magnetic field strength – they did not provide information on vector direction. In addition, the waveform in Figure 1 was derived by subtracting the ambient geomagnetic field magnitude from the measured field magnitude:

$$\Delta B = B_{measured} - B_{amb} \qquad\qquad \text{EQ. 1}$$

This subtraction is the reason for the negative field values in the waveform. Because the perturbation magnetic field generated by burst-generated currents is a small fraction of the ambient geomagnetic field, the derived difference field can be approximated as:

$$\Delta B \cong \overrightarrow{\delta B} \cdot \vec{B}_{amb} / B_{amb} \qquad\qquad \text{EQ. 2}$$

where $\overrightarrow{\delta B}$ is the perturbation magnetic field vector. This means that the derived difference field only provides information about the component of the perturbation magnetic field that is parallel to the ambient magnetic field direction. In addition, positive values indicate a perturbation magnetic field that is parallel to the geomagnetic field, while negative values indicate that the fields are antiparallel.
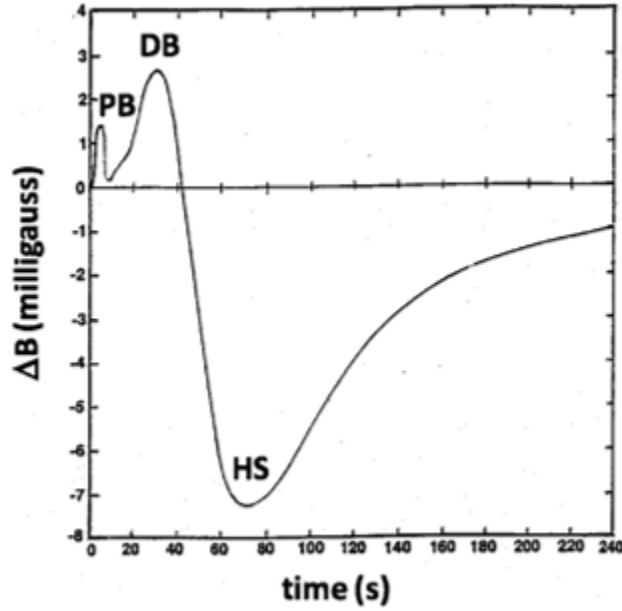
**Figure 1. Magnetic field profile at Johnston Island
following Starfish event, as measured by P. Dyal.**

The labels in Figure 1 correspond to Longmire's identification of the relevant physics in each phase of the waveform: propagated blast wave (PB), diffused blast wave (DB), and heave signal (HS). PB is due to the electromagnetic signal that diffracts around the edge of the X-ray patch and down to the ground. DB is due to the magnetic bubble field that diffuses directly downward through the X-ray patch. As we will show later in this report, our analysis of numerical simulation results suggests that the positive excursion that Longmire identifies as DB is more likely a part of the heave signal (HS) as opposed to a debris-driven magnetic bubble effect (E3A). Other researchers have suggested a similar attribution [3].

2   THEORY OF E3B WAVEFORMS

2.1   Heave Current Circuit

A key concept for understanding E3B waveforms is the heave current circuit. Figure 2 diagrams the standard picture of heave current generation and closure. Rising plasma in the burst-created fireball acts as a dynamo while beta-patch ionization acts as a load. These two elements are connected by currents (purple lines in the figure) that flow parallel to magnetic field lines (red) on the east and west sides of the fireball. Arrowed blue curves show the ground electric field pattern associated with this simplified current circuit. Note that the ground electric field has a two-cell, "double-bullseye" pattern oriented such that the electric field below the burst is predominantly directed towards the east.

3
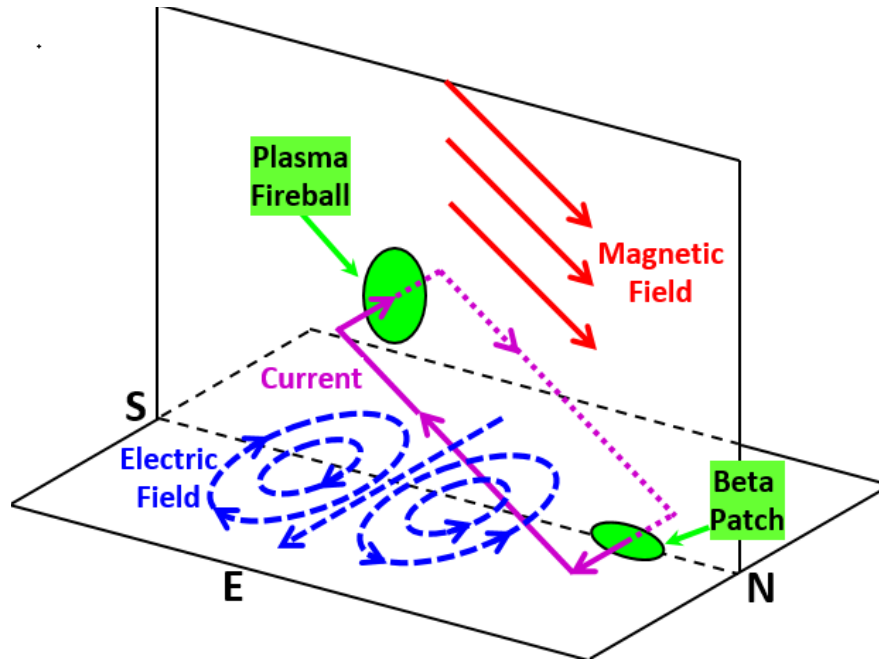
Figure 2. Schematic of heave current circuit.

The importance of the beta patch in the heave current circuit stems from the enhanced conductivity it creates within the X-ray patch. In the absence of the beta patch, heave currents will still close in the X-ray patch, but closure will be more diffuse and thus alter the E3 signal at the ground. Figure 3 shows color contours of conductivity overlaid with perturbation magnetic field vectors from a typical first-principles numerical simulation of E3. The plotting plane is a magnetic meridian (like the vertically-oriented plane in. Figure 2) with magnetic north on the right. Orange color contours delineate the high-conductivity beta patch and green contours delineate the X-ray patch. Yellow arrows indicate the direction of the ambient geomagnetic field.
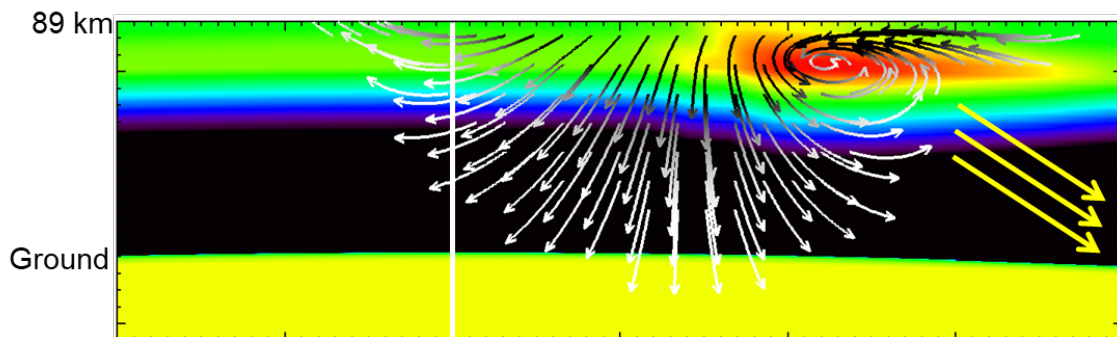
Figure 3. Perturbation magnetic field vectors from heave current closure through beta patch.

The perturbation magnetic field pattern has a circulation center within the beta patch. Application of the right-hand rule indicates that the counter-clockwise circulation corresponds to a focused electric current coming out of the plotting plane, and is thus consistent with the heave current

circuit illustrated in Figure 2. Note that below the beta patch and to the north, the counter-clockwise circulation generates a component of the perturbation field parallel to the ambient field direction ($\overrightarrow{\delta B} \cdot \vec{B}_{amb} > 0$), while south of the beta patch, it is directed anti-parallel ($\overrightarrow{\delta B} \cdot \vec{B}_{amb} < 0$). In addition, the beta patch and its associated perturbation field-circulation pattern drift northward as the fireball rises. Since the derived magnetometer measurements effectively measure the parallel component of the perturbation field, the north-south location of the beta patch relative to the magnetometer location will in general have a positive phase followed by a negative phase as the beta patch moves northward overhead. This predicts a waveform of the type shown in Figure 2, without the need for invoking the concept of a diffused blast wave.

2.2 Hall Conductivity

The standard picture of the heave current circuit neglects effects of anisotropy in the conductivity tensors that characterize burst-generated ionization layers. In general these tensors have both Pedersen (diagonal) and Hall (off-diagonal) components. The off-diagonal components of Hall conductivity are symmetry breaking terms which act to rotate the heave current circuit in the manner shown in Figure 4. Beta patch closure current rotates to have a small southward component (exaggerated in the figure for purposes of illustration). This in turn rotates the plane of the parallel current legs that connect the fireball to the beta patch. The rotation is such that the electric current leg returning to the fireball is at a lower altitude than the electric current leg going to the beta patch. The consequence for E3B ground electric field pattern is a rotation of the "bulls-eye" from predominantly eastward directed to predominantly northward directed.
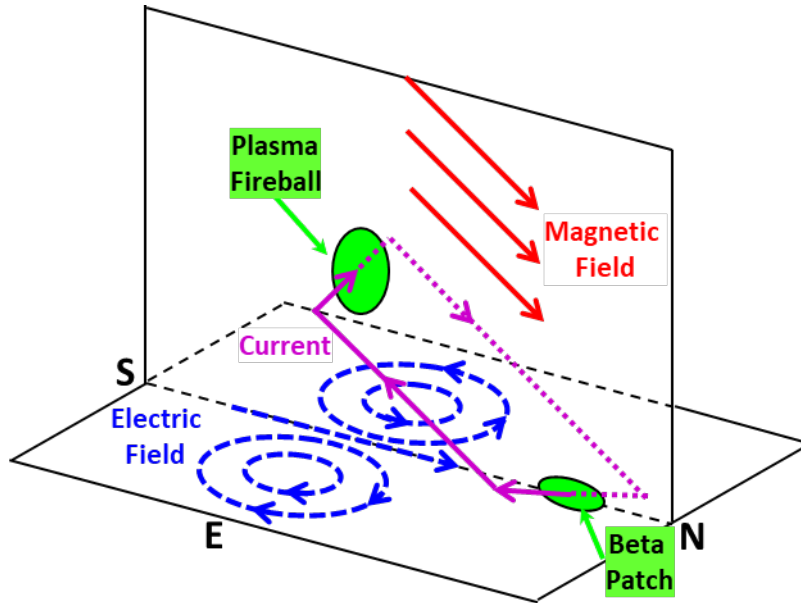
Figure 4. Consequence of anisotropic beta-patch conductivity on the heave current circuit.

Rotation of the ground electric field pattern in the manner shown in Figure 4 has been corroborated with data taken during the Fishbowl test series [4]. Examples of this pattern from numerical simulation will be shown in shown in Section 3.

2.3   Ground Conductivity

For the relatively low frequencies characterizing E3, induced ground electric fields can be represented as a diffusion problem where the characteristic diffusion length is the skin depth. Skin depth depends inversely on the square root of ground conductivity and also inversely on the square root of ground conductivity. Ground conductivity effects are often approximated using a plane wave assumption which is valid when the horizontal scale lengths of the electromagnetic fields are much larger than the skin depth. Under these circumstances and for a uniform ground conductivity, σ, the horizontal electric field is related to the time derivative of the horizontal magnetic field according to:

$$\vec{E} = \frac{1}{\sqrt{\pi\sigma\mu_o}} \int_0^t \hat{z} \times \frac{\partial\vec{B}}{\partial t} \frac{dt'}{\sqrt{t-t'}}$$

EQ. 3

The above relationship is often used to scale electric field magnitudes for different ground conductivities according to the inverse square root of conductivity that appears in the multiplicative constant. While this scaling may be adequate for the large spatial scales of geomagnetic-storm driven electromagnetic fields, it is often inadequate for the smaller spatial scales of nuclear-burst driven E3 fields. Figure 5 shows contour plots of ground electric field magnitude from a numerical simulation of 100 kT at 100 km altitude. The left plot is from a simulation that used a ground conductivity of 1 milli-Siemens/meter (mS/m) and the right from a simulation that used 1,000 mS/m. The contour color bar is scaled to the peak electric field from each simulation (1.4 V/km for the left and 0.16 V/km for the right). Thus the first thing to note is that the ratio of peak field strength is ~9 while the scaling law from EQ. 3 would predict a ratio of ~32. Secondly, the plots also illustrate that ground conductivity affects the horizontal extent of the ground electric field pattern. The shape of the contours is similar, but higher conductivity results in a smaller horizontal length scale.
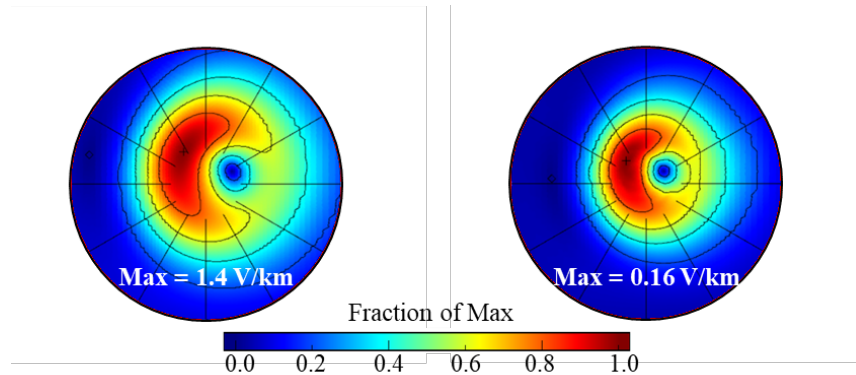
Figure 5. Contour plots of ground electric fields from 100 kT at 100 km and uniform ground conductivity of 1 mS/m (left) and 1,000 mS/m (right). North-South and East-West extents of each plot are 555 km.

3   PARAMETERS AFFECTING E3B WAVEFORMS

In this section we address the weapon parameters that most strongly affect the magnitude, geospatial extent, and vector field pattern of the E3B signal: burst magnetic latitude, altitude, and

yield. Secondary parameters that affect the signal to a lesser degree, and therefore not discussed in this report, include fission yield and X-ray yield and temperature. Fission yield affects E3B through its control of beta-patch conductivity, while X-ray yield and temperature affect E3B through their control of X-ray patch conductivity.

For each of the three parameters, latitude, altitude and yield, we present outputs from sensitivity studies using first-principles numerical simulation. A description of the numerical model can be found in [5]. Outputs will include ground maps of electric field magnitude and vector direction that characterize geospatial extent, as well as electric field waveforms at specific ground locations that characterize time dependence of the E3B signal.

3.1   Magnetic Latitude

Burst magnetic latitude matters for E3B because the angle between the geomagnetic field and the burst vertical determines the strength of the heave generator. At low magnetic latitudes, vertical fireball rise is nearly perpendicular to magnetic field lines making it an efficient MHD generator (see Figure 2). At high magnetic latitudes, rise is nearly parallel to magnetic field lines, significantly reducing generator efficiency. However, as burst magnetic latitude increases, the role of the hot-plasma magnetic-bubble driver discussed in Section 1.1 increases in importance and eventually becomes the dominant driver for E3B. The phenomenology of the plasma bubble driver at higher magnetic latitudes is illustrated in Figure 6. Pressure gradients in the plasma fireball generate a circular diamagnetic current that flows in a direction to restrain expansion (counter-clockwise when viewed from above). Diamagnetic currents create the magnetic bubble and in addition create a time-dependent magnetic field at the ground that induces an electric field. Induced electric field acts to oppose the change in magnetic field (Lenz's Law) and so is directed clockwise during bubble expansion (as shown in the figure) and counter-clockwise during collapse.
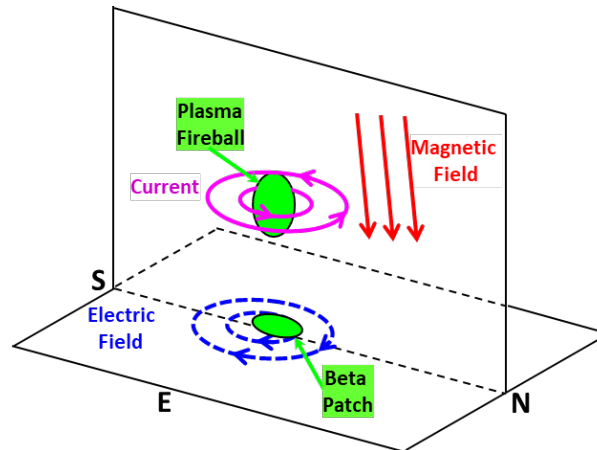
Figure 6. Schematic of diamagnetic current circuit

3.1.1   Ground Maps

For the following sensitivity study we used three burst magnetic latitudes: 14.5º, 31.6º, and 48.8º (the last corresponding to CONUS). All simulations were performed with a single yield of ~100 kT at a burst altitude of 100 km and a uniform ground conductivity of 1 mS/m.

Figure 7 contains geospatial maps of ground electric field magnitude for the three burst latitude cases (rows) at three different times (columns). Burst latitude increases from the top row to the

bottom row. Time increases from left to right with the leftmost column containing plots at the time of peak electric field strength (40 s for the lowest latitude and 20 s for the other two latitudes).
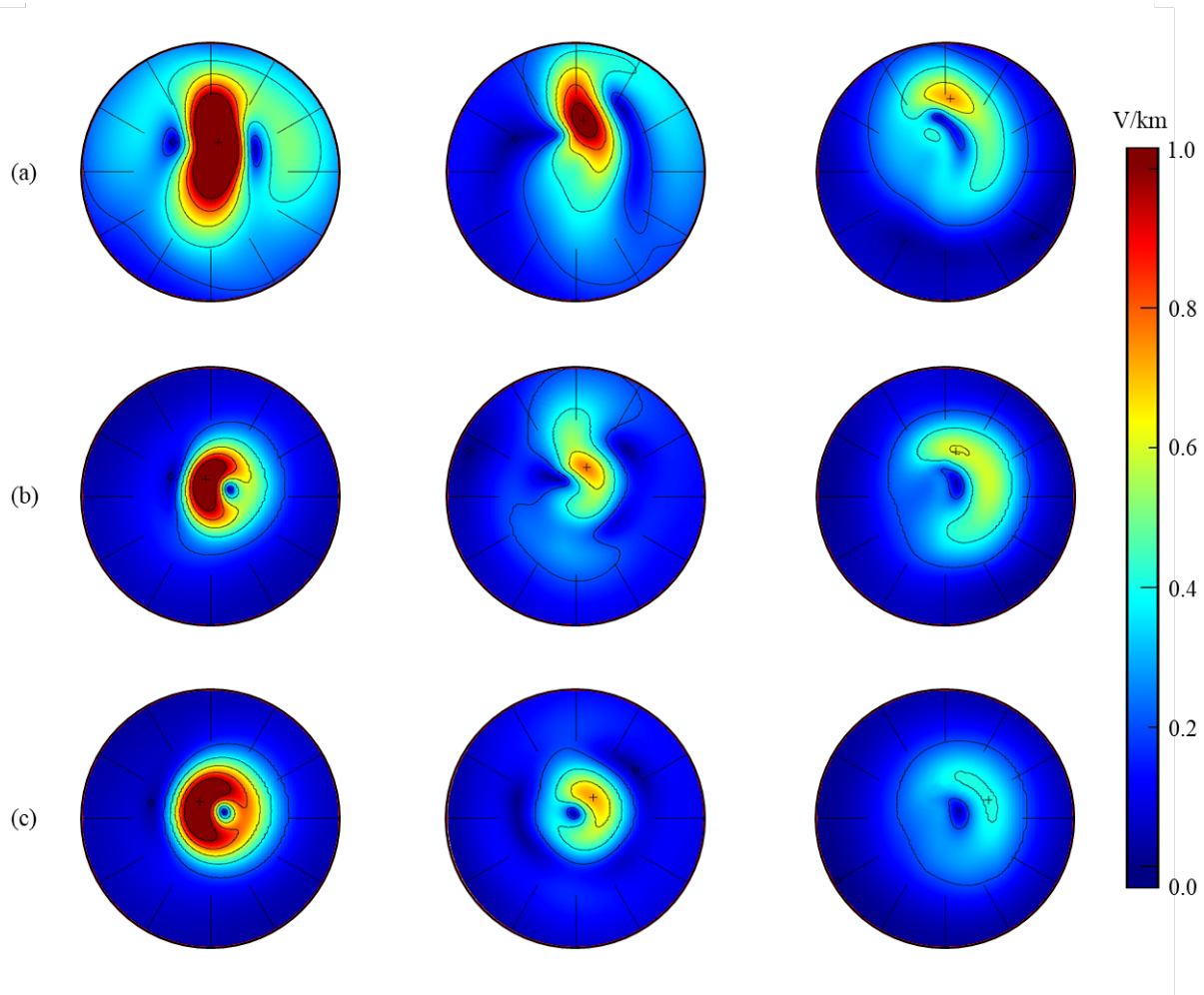
Figure 7. Ground electric field magnitudes from latitude sensitivity study:
(a) burst magnetic latitude = 14.5º at 40, 60, and 90 s (left to right);
(b) burst magnetic latitude = 31.6º at 20, 60, and 90 s (left to right);
(c) burst magnetic latitude = 48.8º at 20, 60, and 90 s (left to right)

Center and right columns are at 60 s and 90 s respectively. Magnetic north is located at 1200 hours in each plot. North-South and East-West spatial extents of each plot is 1,110 km. Figure 8 contains electric field vector plots for the same matrix of simulations / times.
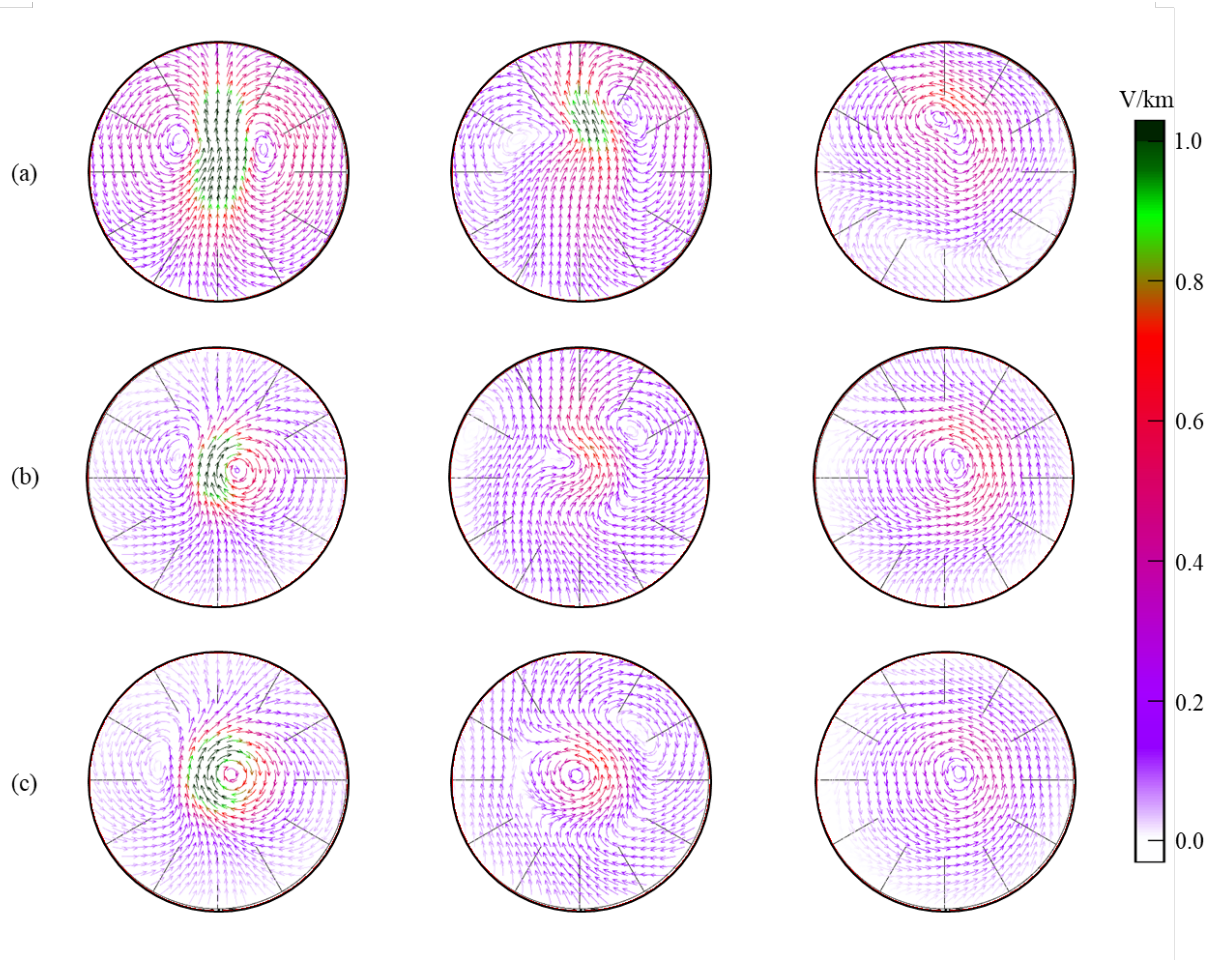
Figure 8. Ground electric field vectors from latitude sensitivity study:
(a) burst magnetic latitude = 14.5º at 40, 60, and 90 s (left to right);
(b) burst magnetic latitude = 31.6º at 20, 60, and 90 s (left to right);
(c) burst magnetic latitude = 48.8º at 20, 60, and 90 s (left to right)

As shown in Figure 8a, the electric field pattern at the time of peak field strength (leftmost plot) is a "double-bullseye" with peak fields directed primarily northward. This pattern is consistent with the physical picture presented in Figure 4 of a heave current circuit in the presence of an anisotropic beta-patch conductivity. The pattern distorts at later times and eventually becomes dominated by a single counter-clockwise circulation cell.

The high-latitude pattern in Figure 8c is dominated by a single clockwise circulation cell at the time of peak field strength (leftmost plot). This pattern is consistent with the physical picture presented in Figure 6 of an induced ground electric field from an expanding magnetic bubble. The pattern reverses polarity at later times as the bubble collapses and becomes a single counter-clockwise circulation cell.

The medium-latitude pattern in Figure 8b is intermediate between the low and high latitude cases. Polarity reversal occurs later than for the high-latitude case.

The electric field magnitude plots of Figure 7 indicate that peak field strength is largest for the lowest latitude case – 2 V/km versus ~1.4 V/km for the medium and high latitude cases. In addition, peak field strength occurs later for the low latitude case– 40 s versus 20 s for the medium and high latitude cases. These features will be further explored with waveform plots that we consider next.

3.1.2 Electric Field Waveforms

Figure 9 shows peak electric field as a function of time for the three burst-latitudes considered for this sensitivity study. Peak electric field is not a single point measurement, but rather is evaluated wherever the peak electric field occurs within the modeling domain. As seen in Figure 7, the location of the peak field changes as a function of time. A discontinuous change of the evaluation point can give rise to cusp-like features in the peak-field waveform such as the one present in the high-latitude waveform (blue curve) just after 40 s. The two maxima on either side of the cusp are caused by magnetic bubble expansion and bubble collapse respectively. As discussed in the previous section, the transition from one maximum to another is accompanied by a reversal of electric field polarity. Subsequent oscillations after 100 s may be numerical artifacts due to electromagnetic waves reflecting off of grid boundaries instead of being transmitted through them.
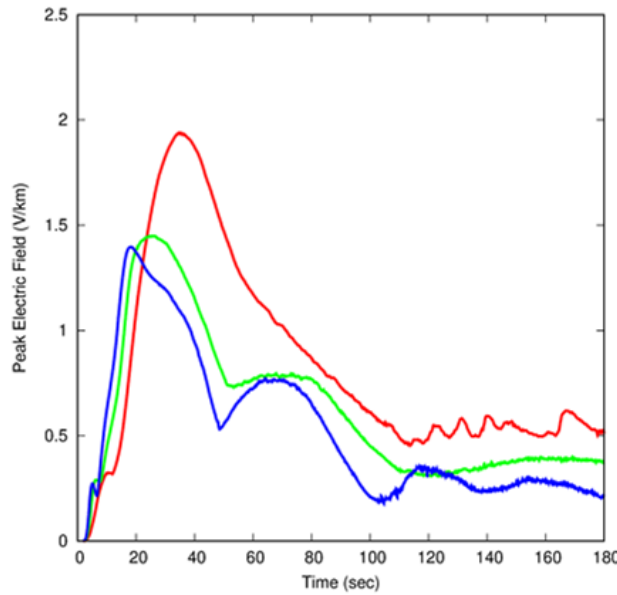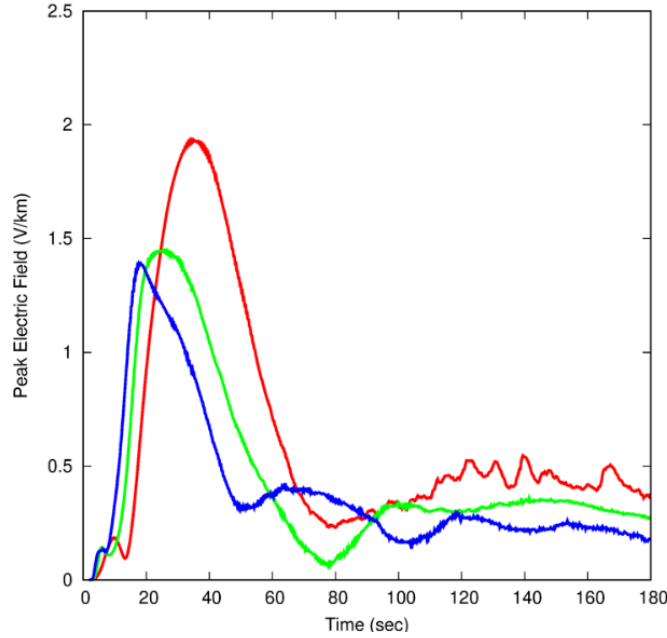

Figure 9. Variation of peak electric field waveforms with burst magnetic latitude: 14.5º (red), 31.6º (green), 48.8º (blue).

The peak waveform for the low-latitude case (red curve) does not have a double maximum separated by a cusp, but instead consists of a single maximum. Since it is driven by a different generation mechanism (heave currents versus diamagnetic currents), it is a fundamentally different waveform. It reaches its maximum value at ~40 s whereas the maximum for the high-altitude waveform occurs at ~20 s. As with the high-latitude case, oscillations that occur after 100 s may be numerical artifacts.

The medium latitude case (green curve) exhibits a shallower cusp depth than the high-latitude case and reaches its maximum value later in time. Both of these features are consistent with a transition between bubble and heave phenomenologies.

Figure 10 shows electric field waveforms extracted at a single point location for the three latitude cases. The chosen point is the location of the maximum electric field over the entire space-time modeling domain. These curves thus provide representations of worst-case waveforms that would be measured by a single ground station.

Figure 10. Variation of single-location electric field waveforms with burst magnetic latitude: 14.5º (red), 31.6º (green), 48.8º (blue).

Figure 11 summarizes E3 scaling with burst magnetic latitude. Peak electric field (left panel) is largest at low magnetic latitudes where the heave driver is dominant. At higher latitudes, the diamagnetic driver becomes dominant and because it is insensitive to latitude, the peak field scaling curve flattens. The time to reach peak field (right panel) shows a greater sensitivity to latitude, but should also become insensitive as burst latitude approaches the magnetic pole.
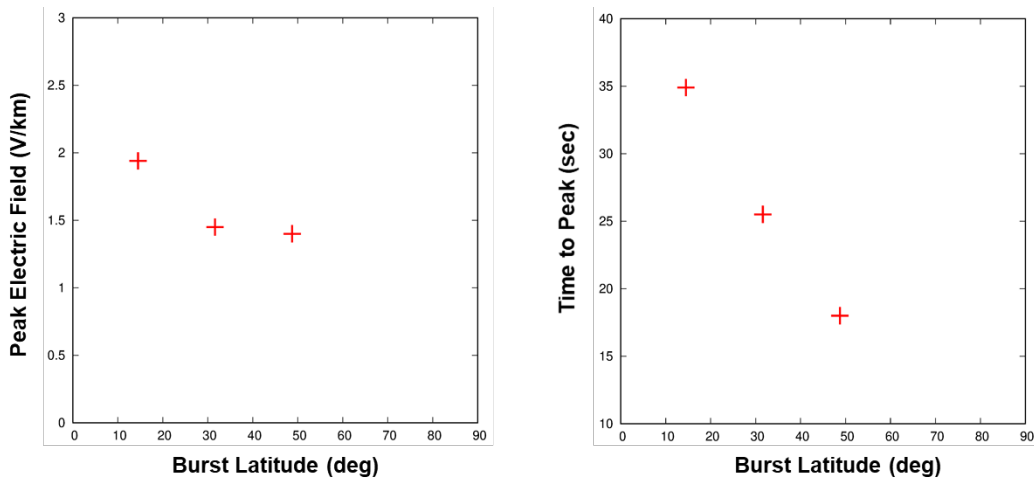
Figure 11. Scaling of peak electric field (left) and time to reach peak (right) with burst magnetic latitude.
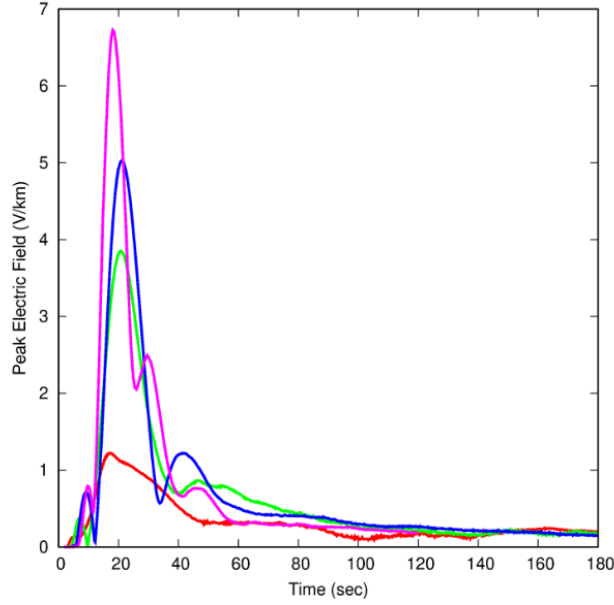
3.2 Burst Altitude

The altitude sensitivity study consisted of burst altitudes of 100, 120, 150, and 200 km. All simulations used a burst yield of 100 kT at a magnetic latitude of 48.8º (CONUS). Figure 12 shows peak electric field waveforms from the altitude study.
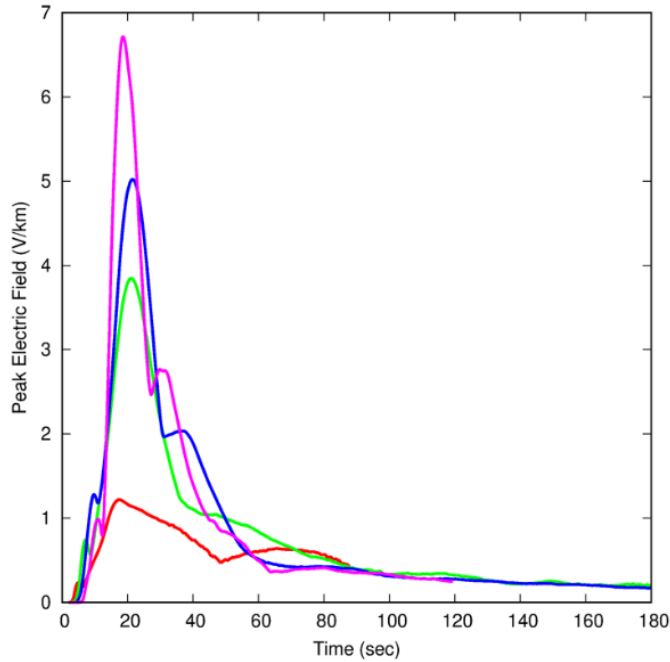
Figure 12. Variation of peak electric field waveforms with burst altitude:
**100 km (red), 120 km (green), 150 km (blue), 200 km (magenta).**

The main altitude dependence is the increase of the maximum field strength with burst altitude. Since the altitude study was performed at the high-latitude node of our simulation matrix, the ground electric field patterns for these cases are similar to those shown in Figure 8c, with a first maximum occurring during clockwise circulation polarity followed by a polarity reversal and a second maximum.

Figure 13 shows electric field waveforms extracted at a single point location for the four altitude cases. As before, the chosen point is the location of the maximum electric field over the entire space-time modeling domain. Cusps in these waveforms arise as minimum field regions move over the evaluation point; however, the overall evolution time-scale is similar to the peak field waveforms.

**Figure 13. Variation of single-location electric field waveforms with burst altitude:
100 km (red), 120 km (green), 150 km (blue), 200 km (magenta).**

Figure 14 summarizes E3 scaling with burst altitude. Peak electric field (left panel) increases with burst altitude, but the rate of increase (slope of the curve) is decreasing, suggesting saturation or maxima for burst altitudes above 200 km. These results are consistent with the dependence of diamagnetic bubble evolution on burst altitude. As burst altitude increases, atmospheric density decreases, resulting in faster plasma expansion and larger diamagnetic bubbles. The stronger driver competes with increasing distance between driver and ground which acts to reduce signal strength. These competing effects are also the likely reason that the time to reach peak field (right panel) exhibits a maximum at a burst altitude of 150 km. An important difference between our result and previous numerical studies [6] is the monotonic increase of peak field up to burst altitudes of 200 km. Numerical studies in [6] predict an E3B signal maximum at a burst altitude of 150 km. It is important to note that the burst-altitude scaling in Figure 14 is restricted to the single CONUS burst-latitude used for all the altitude simulations of this study. Since the E3B driver for low-latitude bursts (heave) is a fundamentally different driver than for high-latitude bursts (diamagnetic), it is likely that burst-altitude scaling will also be different.
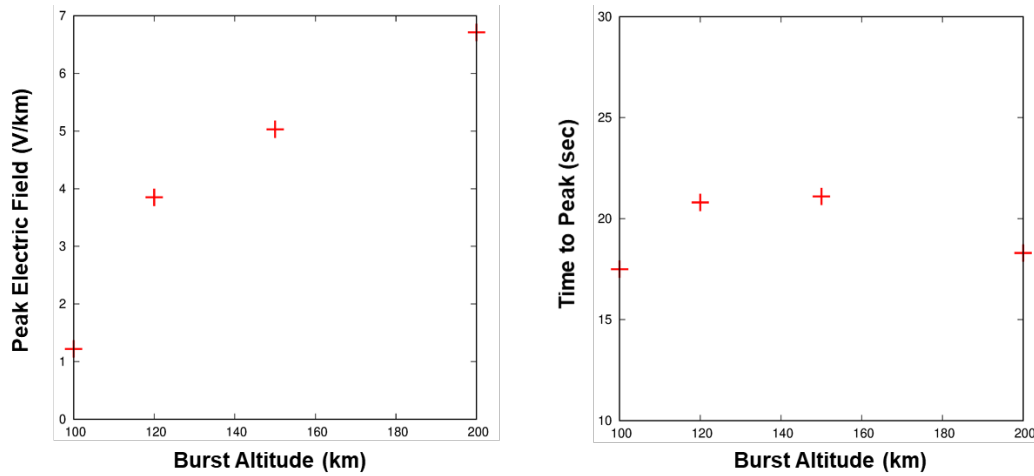
**Figure 14. Scaling of peak electric field (left) and
time to reach peak (right) with burst altitude.**

3.3   Yield

The yield sensitivity study consisted of simulations using 10, 20, 50, 100, 300, and 1,000 kT. All simulations used a burst altitude of 150 km at a magnetic latitude of 48.8º (CONUS). Figure 15 and Figure 16 show peak electric field waveforms from the yield study. As expected, maximum electric fields increase with burst yield. The time to first maximum and time between first and second maximums also increase with burst yield.
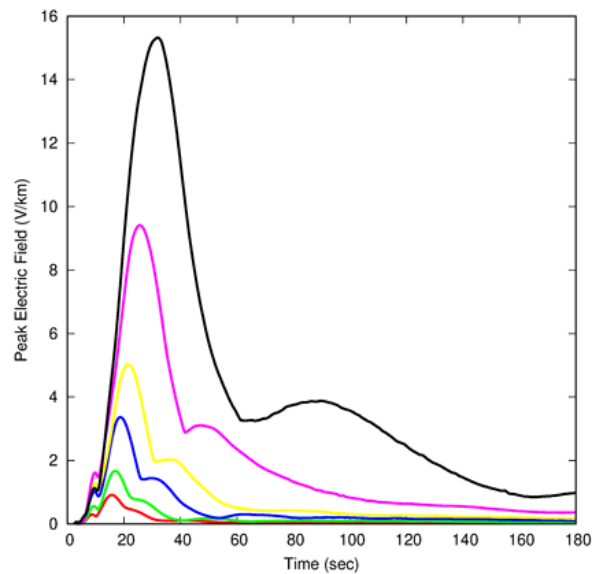

**Figure 15. Variation of peak electric field waveforms with burst yield:
10 kT (red), 20 kT (green), 50 kT (blue), 100 kT (yellow),
300 kT (magenta), 1,000 kT (black)**
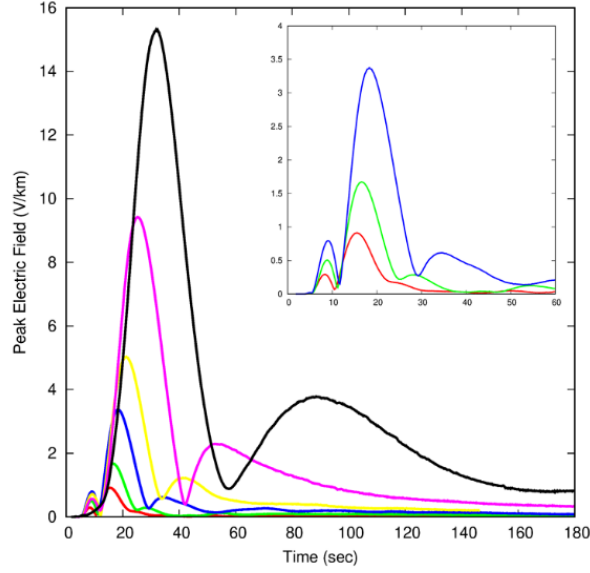
**Figure 16. Variation of single-location electric field waveforms with burst yield:
10 kT (red), 20 kT (green), 50 kT (blue), 100 kT (yellow),
300 kT (magenta), 1,000 kT (black). Inset magnifies lowest yield cases.**

Figure 17 summarizes E3 scaling with burst yield. Both peak electric field (left panel) and time to reach peak field (right panel) appear to be approaching asymptotic limits. E3 signal saturation with yield is also predicted in [6]; however, there the yield at which saturation occurs is 100 kT whereas saturation does not occur until after 1,000 kT in our study.
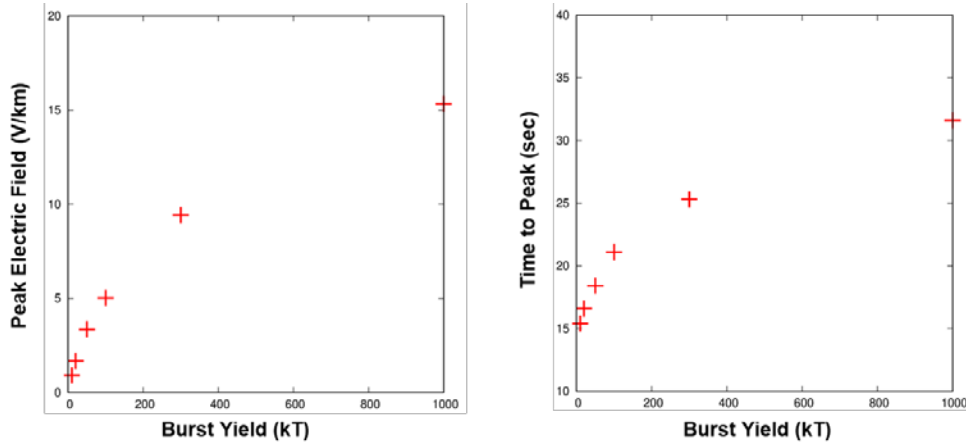
**Figure 17. Scaling of peak electric field (left) and
time to reach peak (right) with burst yield.**

In addition to maximum electric field magnitude, another important difference in ground electric fields from different burst yields is the spatial scale of the fields. Figure 18 illustrates this with ground electric field maps from the 20 kT and 1 MT cases of the yield sensitivity study.

15
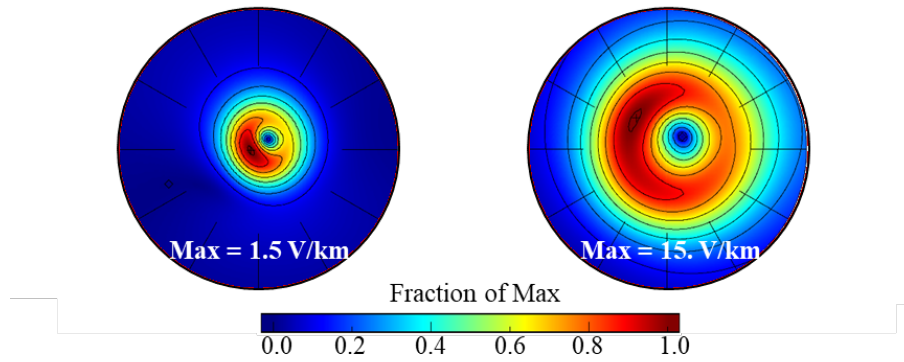
Figure 18. Ground electric field maps from 20 kT case (left) and 1 MT case (right) illustrate differences in maximum field strength and spatial extent. East-West and North-South extents of each plot are 1,110 km.

4   SUMMARY AND CONCLUSIONS

E3B has historically been understood as the heave-driven component of E3. First-principles simulation reveals an important additional driver associated with expansion of the burst-generated plasma fireball. This diamagnetic driver becomes the dominant driver as the heave driver weakens at higher burst magnetic latitudes. Whereas the ground electric field patterns from low-latitude heave-driven E3B are characterized by a "double-bullseye", field patterns from higher-latitude diamagnetically-driven E3B are characterized by a single circulation cell that weakens and then re-brightens with opposite polarity. We attribute this pattern morphology to diamagnetic bubble expansion and collapse. The presence of the diamagnetic driver complicates the latitude dependence of E3B, affecting latitude scaling of peak electric field strength, time to reach peak field, and electric field direction. We find peak fields from heave-driven E3B are larger than those from diamagnetic-driven E3B by about 25%.

Our study of E3B altitude scaling was conducted at a burst magnetic latitude of 48.8° in the diamagnetically-driven regime. We find that the increase in driver strength with burst altitude that results from faster magnetic bubble expansion, offsets the reduction in ground field strength from increasing distance between driver and ground, and yields a peak field that monotonically increases with burst altitude over the range of our study (maximum burst altitude of 200 km). Peak field strength for a burst altitude of 200 km was about a factor of 6 larger than peak field strength for a burst altitude of 100 km. Additional simulations would be required to determine where the altitude scaling curve reaches its maximum value before turning over. In addition, performing the same altitude study at a low burst magnetic latitude will likely produce a different altitude scaling due to differences in the respective drivers (heave versus diamagnetic).

E3B yield scaling exhibits increasing peak field strength with yield that asymptotically approaches a saturation value. Our results suggest that peak fields are still increasing at the maximum yield of 1,000 kT used in our study. For this maximum yield we find the largest peak field of our study of ~15 V/km (for a ground conductivity of 1 mS/m). As expected, we also find that the spatial extent of the E3 ground field pattern increases with burst yield.

16

5 REFERENCES

1. Dyal, P. (2006), *Particle and field measurements of the Starfish diamagnetic cavity*, J. Geophys. Res., 111, A12211, doi:10.1029/2006JA011827.

2. Longmire, C. (1995), *Present status of MHD EMP calculations*, Unpublished Report.

3. Sloan, M.L., J.R. Thompson, and C.S. Kueny (1994), *Comparison of MHDEMP heave simulation predictions with STARFISH, KINGFISH and CHECKMATE nuclear test data*, Austin Research Associates, Report No. I-ARA-94-U-22.

4. Siebert, K., E. Witt, J. Schoendorf, R. Nep, G. Jones (2014), *First-principles E3 modeling: code validation*, HEART Technical Interchange Meeting 2014.

5. Siebert, K. et al (2017), *High-altitude nuclear effects modeling and simulation upgrades (HANEMS) final report*, DTRA-TR-17-32.

6. Gilbert, J., J. Kappenman, W. Radasky, E. Savage (2010) *The late-time (E3) high-altitude electromagnetic pulse (HEMP) and its impact on the U.S. power grid*, Meta R-321.